NASH Pharmacology at WuXi AppTec

Biology Business Unit, Research Service Division, WuXi AppTec (Shanghai) Co., Ltd.

2019

Content

1. Nonalcoholic Steatohepatitis (NASH)

NASH is multifactorial disease with complex etiology, of which a large part is to be understood. Diet and life-style induced hepatic steatosis is the primary factor in the development of NASH. Metabolic changes and stresses result in hepatic inflammation and cellular damages, followed by fibrosis, which progressively leads to cirrhosis and eventually hepatic cellular cancer. Histopathology remains the diagnostic standard of NASH (Fig. 1.1), characterized by steatosis, inflammation, ballooning and fibrosis, corresponding to the underlining physiological changes mentioned above.

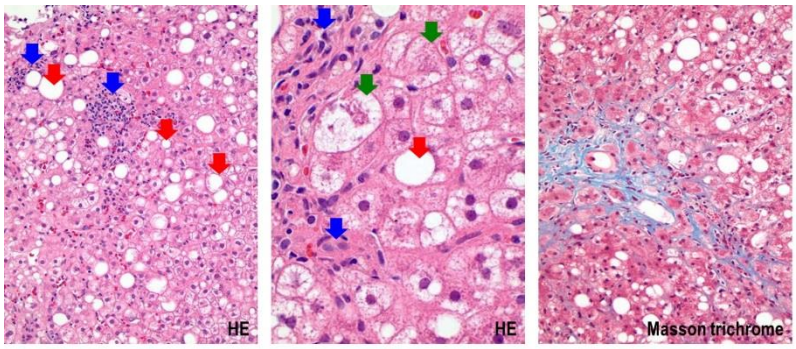

Figure 1.1. Histopathology of human liver of NASH (source: Medscape). Red arrows indicate steatosis (accumulation of fat droplets inside hepatocytes); blue, infiltration of lymphocytes; and green, ballooning of hepatocytes. Fibrosis is readily shown in the right panel.

Despite the prevalence of NASH, no therapeutic treatment has been approved by FDA for its treatment. Table 1 lists compounds that are in the different phases of clinical trial for the NASH indication. They are grouped according to their mechanisms of action as modulators of metabolism, inflammation and fibrosis, and all possible combinations.

Table 1. INDs in different clinical trial phases for NASH indication (source: clinicaltrials.gov).

	Phase I	Phase II	Phase IIb	Phase III
Metabolic	BFKB8488A (Genentech); CER209 (Cerenis); EYP001 (Enyo); HM15211 (Hanmi); MK-3655 (NGM/Merck); PF-07055341 (Pfizer); TERN-101 (Terns)	EDP-305 (Enanta); Gemcabene (Gemphire); LIK066 (Novartis); LMB763 (Novartis); PF-06835919 (Pfizer); PF-06865571/PF-05221304 (Pfizer); PF-05221304 (Pfizer) ; SAR425899 (Sanofi);	BMS-986036 (BMS); MSDC-0602K (Cirius); Semaglutide (Novo Nordisk); Tropifexor (Novartis)	**Obeticholic acid** * (Intercept)
Inflammatory	BI1467355 (BI); Foralumab (Tiziana); GRI-0621 (GRI Bio); Namodenoson (Can-Fite); SGM-1019 (Second Genome)		Emricasan (Conatus/Novartis); IMM-124E (Immuron)	
Fibrotic		Apararenone (Mitsubishi); Nitazoxanide (Genfit); Tipelukast (MediciNova)		GR-MD-02 (Galectin)
Metabolic/ Inflammatory		Saroglitazar (Zydus)	Aramchol (Gelmed); **MGL-3196*** (Madrigal); Seladelpar (Cymabay); VK2809 (Viking)	**Elafibranor*** (Genfit)
Metabolic/ Fibrotic		NGM282 (NGM)		
Fibrotic/ Inflammatory				**Cenicriviroc*** (Allergan) **Selonsertib*** (Gilead)
Metabolic/ Inflammatory/ Fibrotic			Cilofexor/firsocostat/selonsertib (Gilead); Lanifibranor (Inventiva); Tropifexor/cenicriviroc (Novartis)	

* Compounds that are tested in a mouse model for NASH, see Section 6 for details.

The Biology Business Unit at WuXi AppTec (Shanghai) has established a Center of Excellence for NASH, dedicated to researches and services of NASH pharmacology, ranging from in vitro target-based and functional assays to in vivo animal models, efficacy tests and mechanistic studies, using the latest technologies such as gene expression profiling by RNA-seq and quantitative histopathology. Most recently, we have expanded NASH animal models from rodents to cynomolgus monkey.

2. In vitro NASH target and functional assays

Based on the compounds in clinical trials (Table 1) and the published literatures, we selected NASH targets and set up direct binding, enzymatic activity, cellular function and reporter assays (Table 2). All of these assays were validated with reference compounds, with IC_{50}/EC_{50} comparable to those in literatures. Figures 2.1 and 2.2 give two examples of such validation. These assays are readily available for HTS and compound profiling. We also accept customer-tailored assays for new targets and those that are not listed in Table 2. We also established in vitro assays for fatty acid induced inflammation (Figure 2.3) and fibrosis (Figure 2.4)

Table 2. In vitro assays for NASH targets

NASH target	protein binding	enzymatic activity	cellular function	reporter
GLP-1R	yes		yes	
DPP4,8,9		yes		
SGTL1			yes	
SGTL2	yes		yes	
SGLT2 (rat)			yes	
ACC1/ACC2		yes		
DGAT1/DGAT2		yes		
HMG-CoA		yes		
FGF21			yes	
SCD1		yes		
PPAR α,β/δ,γ	yes			yes
CCR2			yes	
CCR5			yes	
CXCR4			yes	
PDE4		yes		
ASK1		yes		
SSAO/VAP-1		yes		
FXR	yes		yes	
TGR5			yes	
PXR				yes
KHK		yes		
THR	yes		yes	
TRPV4			yes	

Stable cell line: HEK-GLP-1R, WuXi
Method: Tag-lite assay
Format: 384-well

Stable cell line: HEK-GLP-1R, WuXi
Method: Radioligand filtration
Format: 96-well

Stable cell line: HEK-GLP-1R, WuXi
Method: TR-FRET cAMP assay
Format: 384-well

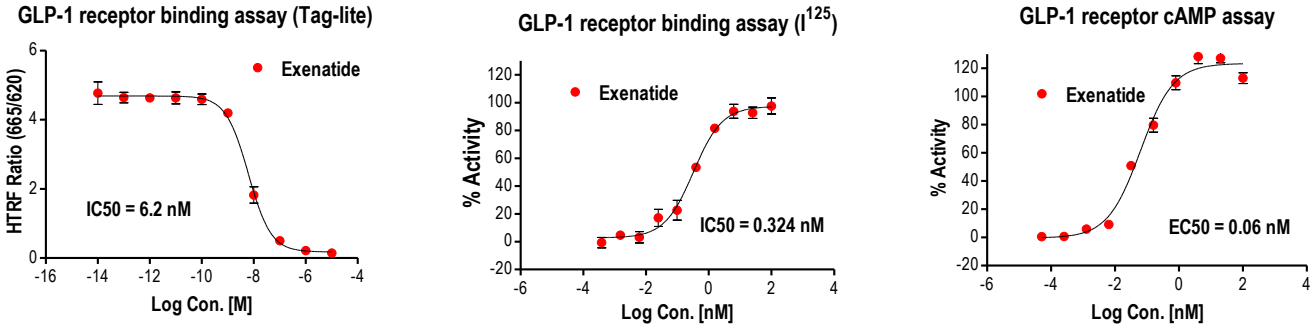

Figure 2.1. In vitro assays for GLP-1R using tag-lite (left), radioligand filtration (center) and TR-FRET cAMP assay (right) in a proprietary stable cell line, HEK-GLP-1R, with IC_{50} and EC_{50} of exenatide indicated. The reported IC_{50}/EC_{50} values of exenatide in these three assays are 8.9/2.8 nM (BJP 160:1973/Cisbio), 0.126 nM (Tocris) and 0.004/0.025 nM (PLoS One 9:387704/Cisbio), respectively.

Enzyme: DPP4
Method: Luminescent assay
Format: 384-well

Enzyme: DPP8
Method: Luminescent assay
Format: 384-well

Enzyme: DPP9
Method: Luminescent assay
Format: 384-well

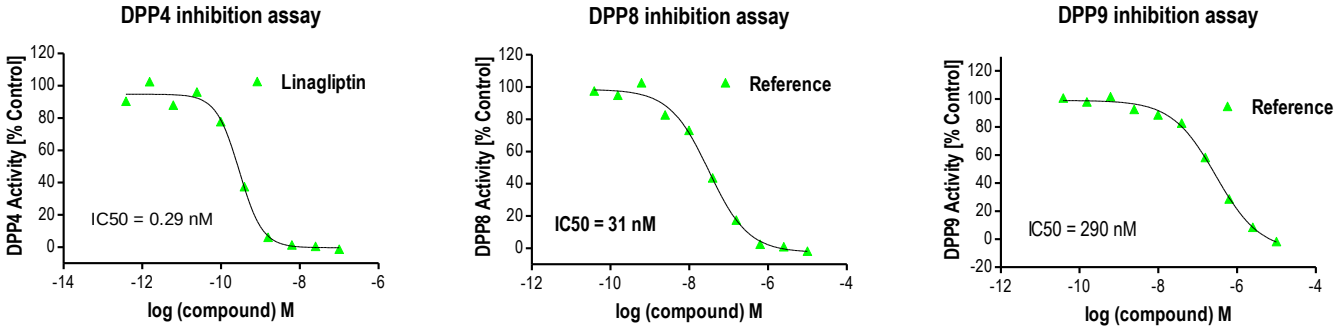

Figure 2.2. Selectivity assays for a DPP4 inhibitor. Ligagliptin was tested in the enzymatic assays of DPP4, DPP8 and DPP9 (left, center and right panels), with IC_{50} indicated. The reported IC_{50} values are 1.0 nM [Tradjenta FDA report (201280Orig1s000)], 50 nM (JMC 54:5737) and 540 nM (JMC 54:5737), respectively.

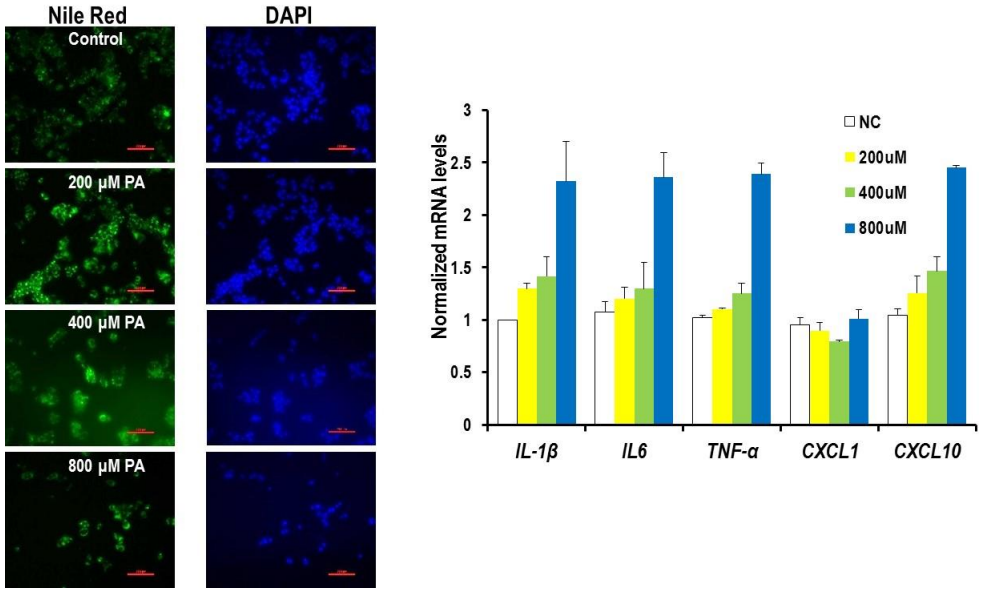

Figure 2.3. Palmitoleic acid induced inflammation in HepG2 cells. Induced cells were stained with Nile red for intracellular accumulation of fatty acid (steatosis, left), and induction of expression of genes for inflammation was analyzed by qRT-PCR (right). At the highest concentration of palmitoleic acid, induction of IL-1β, IL6, TNF-α and CXCL10 was readily detected.

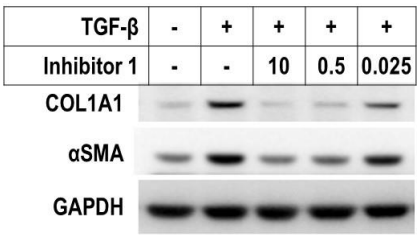

Figure 2.4. TGF-β induced fibrosis in stellate cells. After TGF-β induction, the expression of genes involved in fibrosis, COL1A1 and αSMA, was markedly increased. The induction of gene expression was reversed by an inhibitor of fibrosis.

3. Rodent Models for Steatosis and Fibrosis

We have set up and validated a number of rodent models for steatosis and fibrosis (Table 3). They are classified by the methods used for model construction. Liver histopathology was used verify steatosis, inflammation, ballooning and fibrosis. While nutritional manipulations result in steatosis and inflammation, chemical inductions lead to fibrosis (the sub-anatomical features of fibrosis are different in these models, data not shown) and inflammation, the presence of all three histopathological features was only observed in MCD and HFD+CCL4 models. They were considered as possible NASH models, and characterized further to validate their applicability to in vivo pharmacology of NASH.

Table 3. Rodent models for steatosis and fibrosis, note that these models were all validated with compounds in clinical trials for NASH indications and they have been used for efficacy tests of compounds for steatosis, fibrosis or NASH.

Class	Model	Animals	Histopathological features		
			Steatosis	Inflammation	Fibrosis
Nutritional	HFD	Mouse and rat	Yes	Yes	-
	HFD+G/F[1]	Mouse	Yes	Yes	-
	MCD[2]	Mouse	Yes	Yes	Yes
	HF/CD[3]	Mouse	Hyperlipidemia[3]	Yes	Yes
Chemical	CCL4	Mouse and rat	-	Yes	Yes
	TAA[4]	Mouse and rat	-	Yes	Yes
	ANIT[5]	Rat	-	Yes	Yes
Nutritional + chemical	HFD+CCL4	Mouse	Yes	Yes	Yes
Surgical	BDL	Rat	-	Yes	Yes

Notes: 1. High-fat diet with high glucose and fructose; 2. Methionine and choline deficient diet); 3. High fat and cholesterol diet, only micro-steatosis; 4. Thioacetamide; 5. α-naphthylisothiocyanate; 6. Bile duct ligation.

4. HDF+CCL4 and MCD Models in Mouse

The HFD+CCL4 model is a combination of HFD-induced steatosis/inflammation and CCL4-induced fibrosis/ inflammation, in a sequential manger. Animals are fed on HFD for ~10 weeks. After arriving at the facility, the HFD feeding continues, and at the same time the animals receive 2 i.p. doses of CCL4 every week for 4 weeks. The test compounds are usually administered for the duration of CCL4 treatment (Figure 4.1-A). In the MCD model, steatosis, inflammation and fibrosis are induced concurrently for a total duration of 8 weeks. During the second half of the induction, animals are treated with test compounds at the same time (Figure 4.1-B). Upon completion of in-life experiment, blood and liver samples are collected for biochemical, histopathological [based on the NAFLD activity score (NAS) and fibrosis score used for NASH diagnosis] and gene expression analyses.

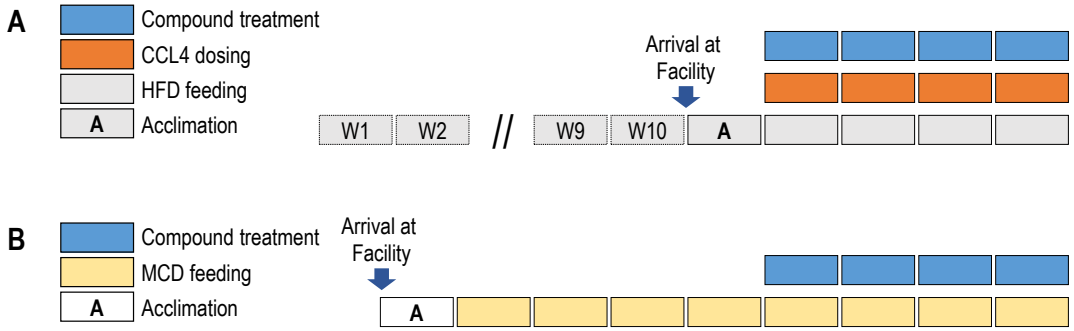

Figure 4.1. HFD+CCL4 (A) and MCD (B) models, in-life procedures for sequential and concurrent inductions, respectively, and compound testing. Each block represents one week duration, with dashed block indicating procedure done by a vender. In both models, compounds are tested at the same time of induction.

We analyzed the two components of the HFD+CCL4 model, namely HFD-induced steatosis and CCL4 induced fibrosis in mouse (Figure 4.2). In the HFD model, steatosis and inflammation were readily observed in the livers. But no fibrosis was evident. CCL4 induced fibrosis and liver damages, including inflammation and ballooning. When HFD and CCL4 were combined, the histopathological features characteristic of NASH were all present in the livers.

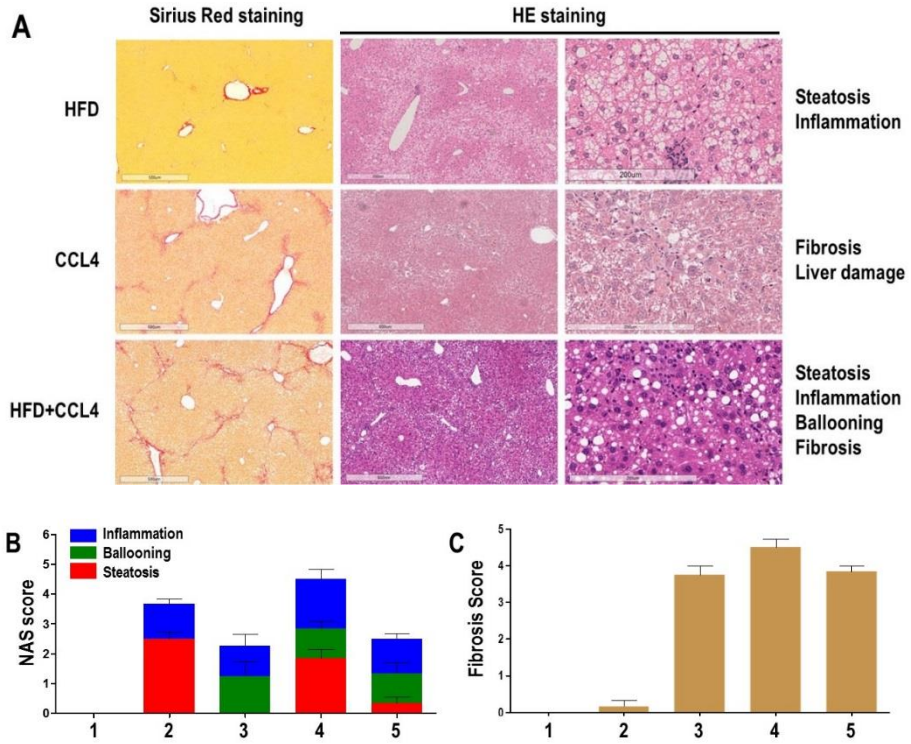

Figure 4.2. HFD+CCL4 model and its pharmacological validation. A. Histopathological analysis of livers of HFD, CCL4 and HFD+CCL4 treatment, with Sirius red staining in the left panel, and HE staining in the center and right panels. NAS (B) and fibrosis (C) scores of Groups 1. Healthy control (fed on regular diet); 2. HFD-induced steatosis and inflammation; 3. CCL4 induced fibrosis and inflammation; 4. HDF+CCL4 induced steatosis, inflammation and fibrosis; 5. Same as 4, with four-week treatment of OCA (30 mpk, p.o., q.d.). The size of each animal group is 10.

Our historical data (>150 animal studies) indicate that, in the livers of HFD+CCL4 model animal, steatosis and inflammation (total score of 3 for each feature) contribute more or less equally to the NAS, whereas balloon (total score

of 2) contributes much less (Figure 4.2-B and data not shown). Usually, a successful model has an average of NAS >4, with four histopathological features readily observed in all individual animals (data not shown). Although CCL4 alone induces significant fibrosis in the livers, the combination of HFD and CCL4 always induces a slightly higher level of fibrosis (Figure 4.2-C and data not shown).

Obeticholic acid (OCA) was used to validate the HFD+CCL4 model. The four-week treatment with OCA significantly reduced the steatosis, and, to a less extent, the inflammation, while the ballooning was largely not effected (Figure 4.2-B). We observed that the ballooning in this model is highly heterogeneous, and the standard diagnostic scoring is not sufficient to capture the efficacy of OCA – see Section 8 for more). The fibrosis in this model was suppressed marginally by OCA. It seems that only the extra level of fibrosis (induced by the combination of HFD and CCL4) is suppressed by this compound (Figure 4.2-C and data not shown, also see Section 7 for more). This is consistent with our results that OCA has no efficacy on CCL4 induced fibrosis (data not shown).

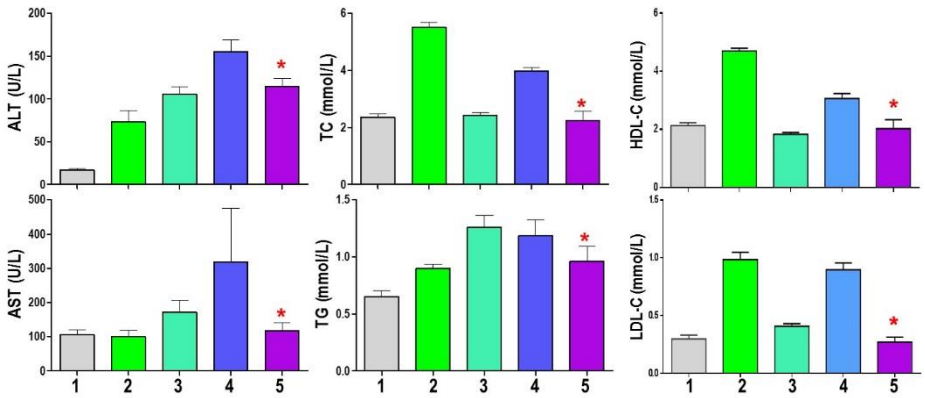

Figure 4.3. Biochemical analyses of serum samples collected on the last day of in-life experiment from: 1. Healthy control; 2. HFD-induced steatosis and inflammation; 3. CCL4 induced fibrosis and inflammation; 4. HDF+CCL4 induced steatosis, inflammation and fibrosis; 5. Same as 4, with four-week treatment of OCA (30 mpk, p.o., q.d.).

The serum sample collected on the last day of the in-life experiment were analyzed for levels of alanine aminotransferase (ALT), aspartate aminotransferase (AST), total cholesterol (TC), triglyceride (TG), high- and low-density lipoprotein-cholesterol (HDL and LDL-C) (Figure 4.3). The levels of serum ALT and AST were accumulative in the HFD+CCL4 model, compared with those in animals treated with HFD and CCL4 alone, whereas the elevated levels of cholesterol in three forms in the HFD+CCL4 model were largely contributed by HFD. TG, on the other hand, stayed more or less at the same as CCL4 induction. OCA reduced the levels of these biochemical indicators in the HFD+CCL4 model, consistent with its role in regulating lipid metabolism, and steatosis and inflammation as seen in histopathological analysis (Figure 4.2)

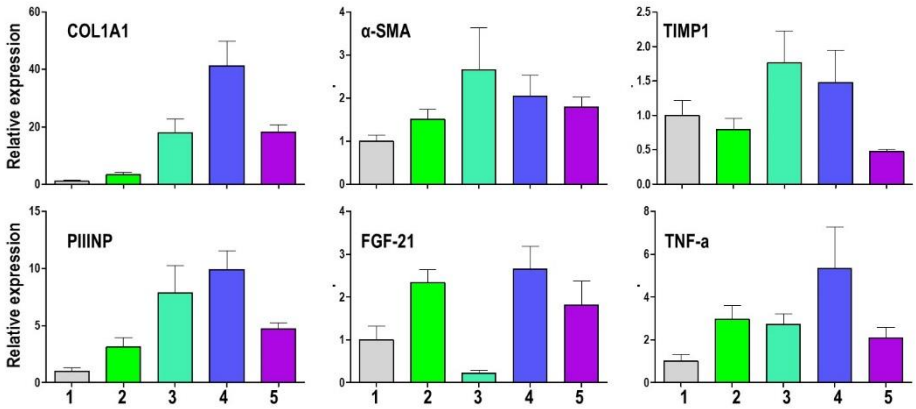

Figure 4.4. Analyses of gene expression in livers from: 1. Healthy control; 2. HFD-induced steatosis and inflammation; 3. CCL4 induced fibrosis and inflammation; 4. HDF+CCL4 induced steatosis, inflammation and fibrosis; 5. Same as 4, with four-week treatment of OCA (30 mpk, p.o., q.d.). The relative gene expression, by quantitative RT-PCR, was normalized by the average of the healthy control.

We then looked at the expression of genes (implicated in NASH and MOA of OCA) in the livers of HFD, CCL4 and HFD+CCL4 animals (Figure 4.4). Of 6 genes examined, COL1A1 was highly induced in the HFD+CCL4 animals, and PIIINP, to a much less extent. Their expression was significantly reduced after the OAC treatment. It has been observed that the up-regulation of COL1A1 expression is a hallmark for fibrosis in this and other NASH animal models and that its down-regulation, in most cases, is an indicator of anti-fibrotic efficacy (data not shown). The expression of α-SMA was marginally induced in the CCL4 animals, and less so in the HFD+CCL4 animals. Likewise, OCA had

marginal effect on its expression. Consistent with known results, the up-regulation of expression of FGF-21 and TIMP1 was down regulated by OCA. However, the induction of FGF-21 expression was attributable to HFD alone, whereas that of TIMP1 CCL4 alone. On other hand, the induction of pro-inflammatory gene TNF-α was relatively highly induced in the HFD+CCL4 animals, and it was suppressed by OCA, consistent with the anti-inflammatory effort of OCA observed in Figure 4.2.

These results collectively suggest that the HFD+CCL4 model is not simply additive of the two constituent components. Whole-genome transcription profiling (RNA-seq) was used to survey the gene expression in the three animal groups and the HFD+CCL4 group treated OCA (Figure 4.5). The relative fold of change (log scale) of gene expression in these animal groups was first normalized with the relative level in the healthy control fed on regular diet. The normalized fold of change of each RNA transcript was then converted to z-score by those of all RNA transcripts of a given animal so that the up- and down-regulation could be compared between different animals and different animal groups. The results of relative expression of genes involved in lipid and fatty acid metabolism and inflammation are shown in Figure 4.5. They further support the aforementioned conclusions, at the whole-genome gene expression level, that the gene expressions in the two constituent models (CCL4 and HFD) are differentially regulated, and that in the HFD+CCL4 model the overall gene expression is quantitatively different from two constituent models.

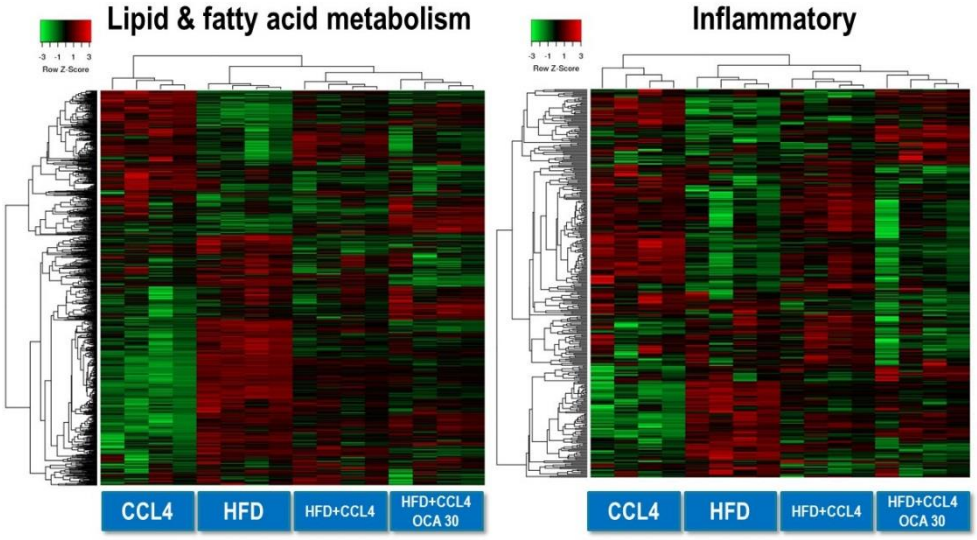

Figure 4.5. Heat maps of relative expression of gene expression in four animal groups of CCL4, HFD, HFD+CCL4 and HFD+CCL4 treated with OCA (30 mpk, for 4 weeks). The z-scores of relative expression of genes involved in lipid and fatty acid metabolism (left) and information (right) were used to construct heat maps, with red indicating up-regulation, and green down-regulation.

In the Phase II clinical trial of OCA, its efficacy in treating NASH was demonstrated by significant improvement in NAS ($\Delta \geq 2$), fibrosis and serum ALT and AST. When OCA was tested in the HFD+CCL4 model, the improvement of steatosis was most pronounced, inflammation to a less extent. However, improvement of ballooning was not observed using the histopathological score system for diagnosis. Nonetheless, the total NAS was significantly improved. Likewise, the improvement of fibrosis by OCA in this model was marginal and restricted to the portion that seems to be induced by the combination of two constituent models, but statistically significant. The improvement of serum biochemical markers by OCA was also demonstrated in this model. Further, the mechanistic aspects of OCA were confirmed by analysis of gene expression in livers. Together our results suggest that the HFD+CCL4 model captures symptoms that are clinically relevant to NASH.

Unlike the sequential inductions in the HFD+CCL4 model, the induction of steatosis, inflammation and fibrosis is simultaneous in the MCD model (Figure 4.1). Animals were fed on MCD (methionine and choline deficient diet) for a total of 8 weeks, during the second half of which animals were treated with several OCA and two other compounds in clinical trial for NASH (Figure 4.6).

Histopathological analysis revealed that steatosis and inflammation are evident in the MCD model, and ballooning to a less extent, and that the fibrosis is also induced (Figures 4.6 and 4.7). However, the fat droplets in the livers of this model is more heterogeneous and larger in size when compared with those found in the HFD+CCL4 model. Likewise, the patterns of fibrosis are different in the livers of these two models (see Section 5).

Two doses of OCA (15 and 30 mpk, q.d., p.o., for 4 weeks) were tested in the MCD model. At the lower dose, neither the steatosis nor the inflammation was improved by the treatment; and the ballooning was exacerbated, resulting in an increase in total NAS. At the higher dose, only steatosis was improved, whereas not only the ballooning but also the inflammation were exacerbated by the OCA treatment. However, the improvement of steatosis was offset by the

increase in inflammation and ballooning. The total NAS scores were not improved by either dose. Likewise, the fibrosis was not improved (Figure 4.7). Evidently, OCA has no efficacy in treating the histopathological symptoms associated with the MCD model, in contrast to what is observed in the HFD+CCL4 model (Figure 4.2-B).

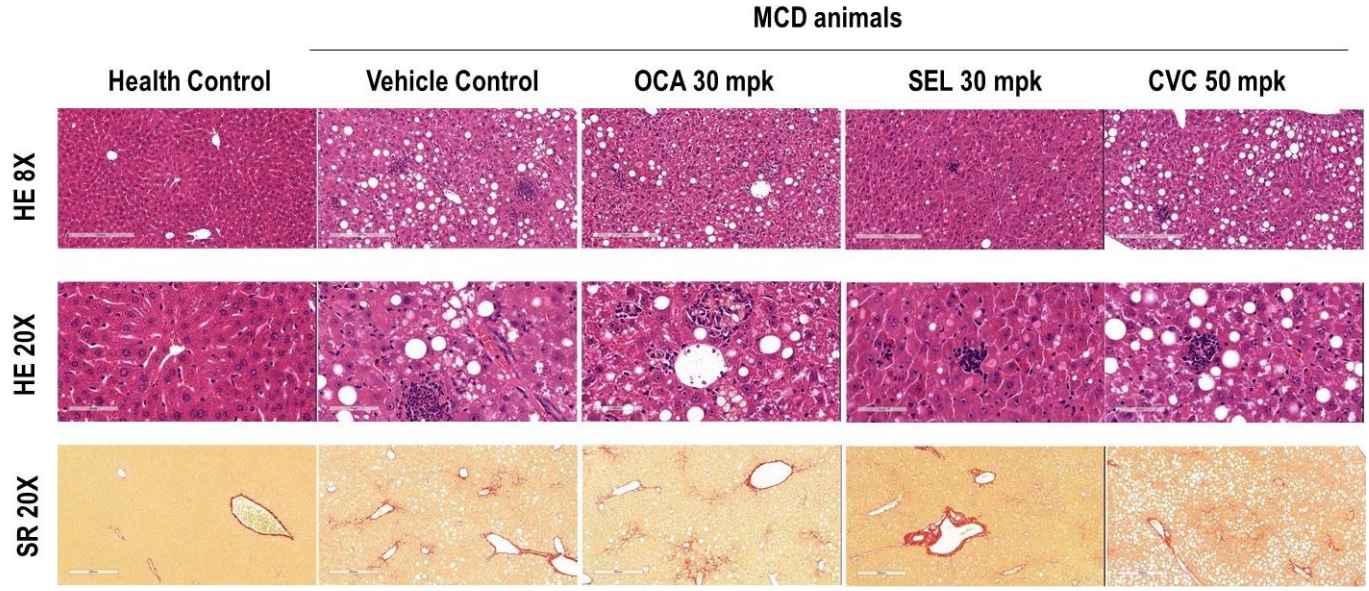

Figure 4.6. Histopathology of livers of healthy control animals and MCD animals treated with vehicle, OCA (30 mpk), selonsertib (SEL, 30 mpk) and cenicriviroc (CVC, 50 mpk). The liver sections were stained with HE and (top and middle rows) and Sirius Red (SR, bottom row). Note that the fat droplets in the MCD model are relatively larger in size and more heterogeneous when compared with the HFD+CCL4 model.

However, selonsertib, at a dose of 30 mpk, displayed efficacy in improving significantly the inflammation and to a less extent the steatosis. The compound was also efficacious in improving fibrosis, in a dose-dependent manner (Figures 4.6 and 4.7). However, the inflammation (and steatosis, to a less extent) was not improved by the compound at two lower doses (3 and 10 mpk) (Figure 4.7A). In other words, selonsertib is efficacious in improving the histopathological symptoms of the MCD model, even though such efficacy is restricted to a higher dose. Cenicriviroc improved the inflammation in the MCD model, and marginally the steatosis. Even though the total NAS is improved by cenicriviroc, the ballooning was exacerbated. The fibrosis was not improved.

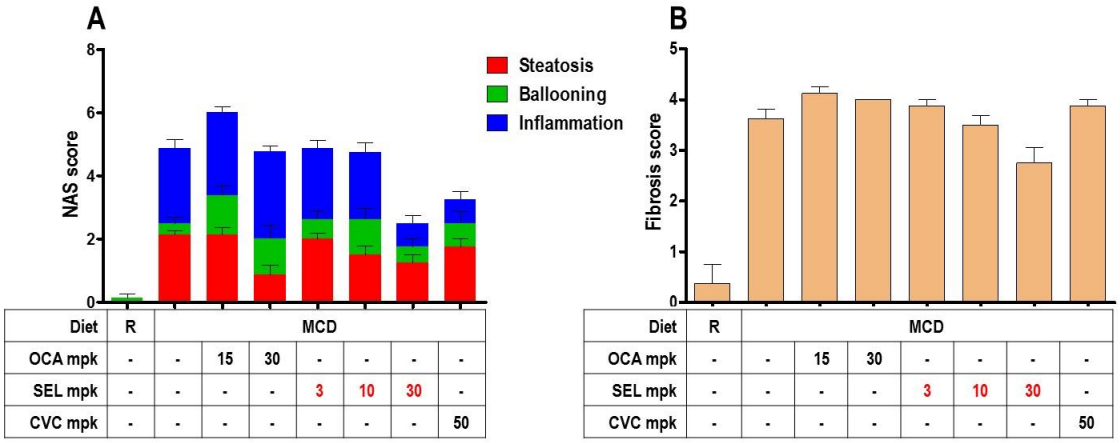

Figure 4.7. Analysis of liver histopathology (A, NAS score; B, fibrosis score) of the MCD model and the treatments of OCA, selonsertib (SEL) and cenicriviroc (CVC). Note that in this model, the steatosis and the inflammation contribute almost equally to the total NAS, and ballooning is not evident, and that the ballooning component of this model responds to NASH compounds (at different doses) differently.

5. Comparison of HDF+CCL4 and MCD Models by RNA-seq Profiling

Our results indicate that the HFD+CCL4 model and the MCD model are different, not only in their liver histopathology (steatosis and fibrosis, most prominently) but also in their response to the treatment of OCA (of the same regimen). This raises the question as to which model is more relevant to NASH. In the first model, the inductions of steatosis and fibrosis are sequentially by HFD and CCL4 (Figure 4.1). Although fibrosis induced by CCL4 is due to liver damage caused by the chemical, we observed that the combination of HDF and CCL4 in the second half of the model induces extra level of fibrosis. The overall fibrosis is perilobular and the fibers between the portal triads (of hepatic artery branch, hepatic vein branch, and bile duct) tend to be bridged, and are more tightly bundled (Figure 5.1). To some extents, the sub-anatomical structures of fibrosis in this model show resemblance to those observed in human NASH livers.

In the MCD model, on the other hand, the hepatic fibrosis seems to radiate from the central veins, and are structurally more amorphous. No bridging fibers were evident in the MCD model (Figure 5.1). In addition, the steatosis in this model is also different – the fat droplets are relatively larger and more heterogeneous and dispersed throughout the hepatic lobules. The induction of steatosis and fibrosis in this model is simultaneous (Figure 4.1). Unlike the HFD+CCL4 model, the depletion of choline in the diet of the MCD model impairs the export of triglyceride from hepatocytes, directly resulting in accumulation of cytoplasmic lipid droplets. On the other hand, the depletion of methionine increases oxidative metabolic stress as methionine is the precursor of glutathione and S-adenosyl-L-methionine (SAM), both of which are antioxidants. It is likely that the forced accumulation of lipid droplets coupled with increased oxidative stress is responsible for the induction of fibrosis in this model.

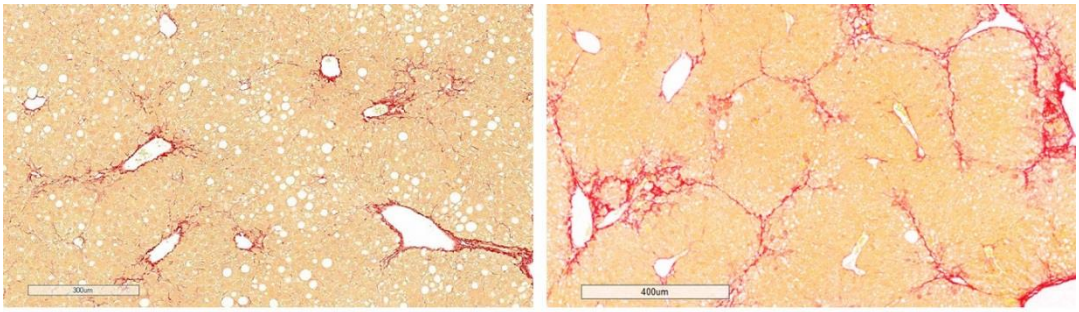

Figure 5.1. Hepatic fibrosis in the MCD model and the HFD+CCL4 model. Note that these two images are displayed at the same scale.

If the underlying causes for steatosis and fibrosis observed in these two models are different, other aspects of these two models should also be different. We used RNA-seq to profile the whole genome expression in livers of both models. When the overall differential expressions (regulated expression normalized by the health control fed on the regular diet, and converted to z-scores) are compared, the correlation coefficient (r) is 0.28. Three sets of gene expressions are selected for comparison (Figure 5.2). For genes involved in lipid metabolism, inflammation and cell cycle regulation, the r values are 0.31, 0.05 and 0.39, respectively, when the two models are compared (Figure 5.2). In particular, the inflammatory responses in these two models are completely unrelated. The comparison of gene expression profiling confirms that these two models are mechanistically different from each other, and that the underlying inflammatory responses in these two models are fundamentally different. Such difference might offer an explanation of the complex pharmacological outcome of different NASH compounds for their effects on inflammation in the MCD model (Figure 4.7).

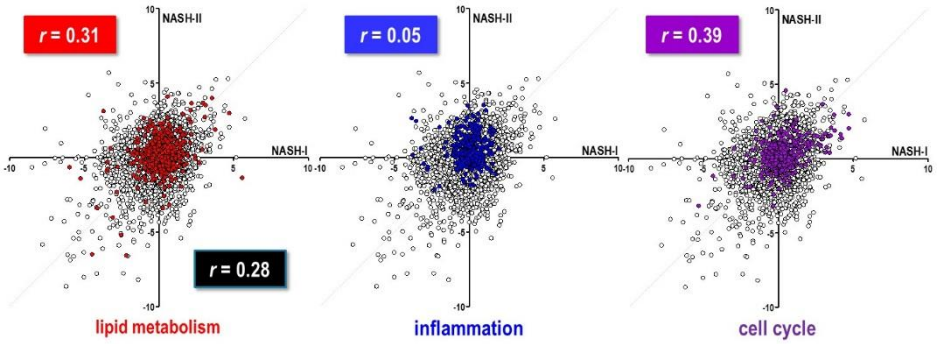

Figure 5.2. Scatter-plots of differential expression of liver genes involved in lipid metabolism, inflammation and cell cycle regulation (colored filled dots) in the context of overall transcriptome (open circles) between the HFD+CCL4 (NASH-I) and MCD (NASH-II) models. Note that the r value in the black box indicates the overall transcriptome, and those in colored boxes respond to genes sets in the same colors.

From histopathological analyses, we demonstrated that OCA is efficacious in the HFD+CCL4 model, but not in

the MCD model. We then examined the gene expressions in response to OCA in these two models (Figure 5.3). Genes involved in inflammatory response and lipid metabolism were selected for this comparison. Despite the overall difference in gene expressions in these two models, we found clusters of genes whose regulation by OCA are preserved in both model (Figure 5.3).

For genes involved in inflammatory responses, half of them are differently expressed in these two models, and OCA has little effect on their expression. However, the genes in cluster A1 are down-regulated in the HFD+CCL4 model but slightly up-regulated in the MCD model, yet OCA up-regulates their expressions in both models. The genes in cluster A2 are slightly up-regulated in the HFD+CCL4 model but down-regulated in the MCD model, in both models their expressions are up-regulated. For the genes in cluster B, their expression are up-regulated in both models, and are down-regulated by OCA (Figure 5.3).

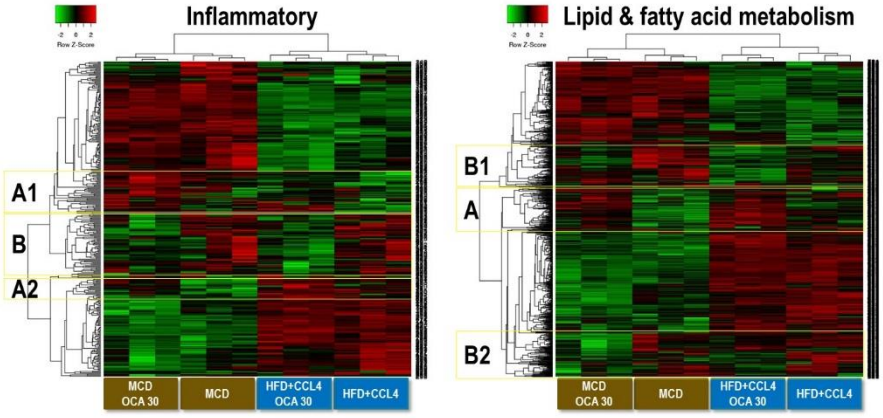

Figure 5.3. Heat-map representation of differential expressions of genes involved in inflammatory response and lipid metabolism in the HFD+CCL4 and MCD models with and without treatment of OCA (30 mpk, 4 weeks). Cluster A and B correspond to genes whose expressions are up- and down-regulated by OCA in both models.

For genes involved in lipid metabolism, most of them are differently expressed in these two models, and OCA has no significant effort. However, genes in cluster A are (slightly) down-regulated in both models, and are up-regulated by OCA. These in cluster B1 are up-regulated in the MCD model and less so in the HFD+CCL4 model. They are down-regulated by OCA in both models. For the genes in cluster B2, their expressions are up-regulated in the HFD+CCL4 model and less so in the MCD model. They are down-regulated by OCA in both models.

These results indicate that the effects of OCA are exerted in both models, and that genes in cluster A and B are mostly likely subject to regulation by OCA. However, since the HFD+CCL4 and MCD models are mechanistically different from each other, the efficacy of OCA could be demonstrated in a model that is (mechanistically) relevant to NASH, in this case, the HFD+CCL4 model.

6. Validation of HFD+CCL4 Model with Compounds in Clinical Trials

Based on the results presented above, the HFD+CCL4 model was designated as an animal model for NASH. To further validate this model pharmacologically, we selected four NASH compounds at different stages of clinical trials, in addition to OCA, and tested them in a 4 week regimen (Table 4). Combinations of OCA with selonsertib, selonsertib with elafibranor, elafibranor with MGL-3196 were also tested in the same manner.

Table 4. NASH compounds selected for validation of the HFD+CCL4 model.

NASH compound (dose)	Target	Clinical Status
Obeticholic acid (OCA, INT-747) (30 mpk)	FXR (agonist)	Completed Phase III, registered as first NASH drug
Elafibranor (ELA, GFT-505) (30 mpk)	PPAR α/δ (agonist)	In Phase III
Selonsertib (SEL, GS-4997) (30 mpk)	ASK1 (inhibitor)	Completed Phase III
Cenicriviroc (CVC, TAK-652) (50 mpk)	CCR2/CCR5 (antagonist)	In Phase III
MGL-3196 (MGL) (30 mpk)	THRβ (agonist)	In Phase IIb

In an independent animal studies, the efficacy of OCA was quantitatively confirmed. In this case, OCA also improved the hepatic ballooning while fibrosis was marginally reduced as observed before (Figure 6.1). MGL-3196 was also efficacious in the model, as it significantly improved steatosis, ballooning and inflammation, and fibrosis in the same manner as OCA (Figure 6.1).

No efficacy was observed with cenicriviroc when tested in this model at 50 mpk. It failed to improve any of the NAS components or fibrosis (Figure 6.1), even though improvement of inflammation was observed in the MCD model (Figure 4.7-A). These seemingly contradictory results are consistent with the demonstration that the inflammatory responses in these two models are mechanistically different (Figure 5.2). Likewise, selonsertib (at 30 mpk) improved the inflammatory response in the MCD (Figure 4.7-A), but if exacerbated the inflammation in the HFD+CCL4 model, with no effects on steatosis (Figure 6.1-A) probably for the same reason. Although the ballooning improved by selonsertib, the fibrosis was not in this model (Figure 6.1-B), contrary to what was observed in the MCD model with the same compound, further suggesting that the fibrosis processes are also different in these two models.

Elafibranor was tested in the HFD+CCL4 model. Consistent with our observation that this compound improves the fibrosis induced by CCL4 alone (data not shown), it improved the fibrosis in this model as well, to a greater extent than OCA and selonsertib (Figure 6.1-B). The ballooning and the inflammation in the HFD+CCL4 model was significantly improved by elafibranor, yet the steatosis was exacerbated at the dose tested (30 mpk), resulting in no significant change in the total NAS score (Figure 6.1-A).

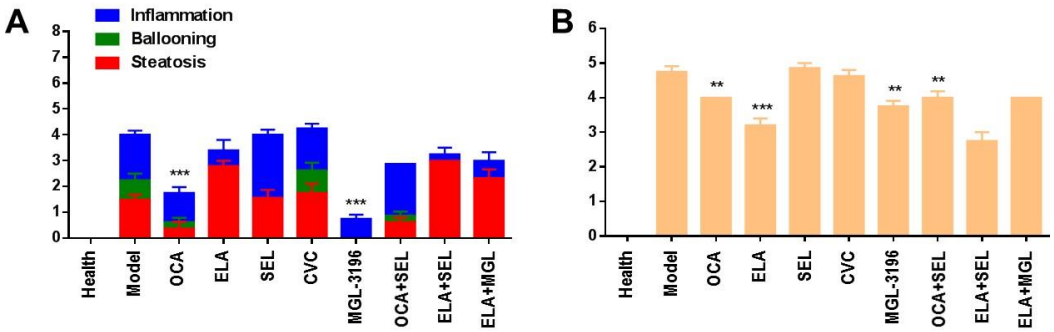

Figure 6.1. Liver histopathology (A, NAS score; B, fibrosis score) of the HFD+CCL4 model after treatment with NASH compounds: OCA, obeticholic acid; ELA, elafibranor; SEL, selonsertib; CVC, cenicriviroc; and MGL, MGL-3196, together with three combinations.

We also tested three combination of OCA with selonsertib, selonsertib with elafibranor, and elafibranor with MGL-3196 (dose of each individual compound, 30 mpk). No synergistic or additive effects were observed with any of these combinations. In the first combination of OCA with selonsertib, the improvement of steatosis and ballooning was preserved. Likewise, the improvement of fibrosis was also preserved. However, the improvement of inflammation (by OCA) was almost ablated (by selonsertib) (Figure 6.1). In the two remaining combinations, the effects of elafibranor were dominant. This is especially true in the combination of elafibranor with MGL-3196 – the improvement of steatosis by the latter was ablated by the former (Figure 6.1-A). However, the anti-fibrotic effect of elafibranor was only preserved in the combination with selonsertib, but not quantitatively with MGL-3196 (Figure 6.1-B). These results demonstrate that, in the HFD+CCL4 model, the net outcome of combinational treatment is not simply additive, nor could be predicted based on the MOAs of compounds in the combination.

7. Quantitative Histopathology of Fibrosis in HFD+CCL4 Model, preliminary results

As noted, in the HFD+CCL4 model for NASH, the CCL4 component is largely responsible for the induction of fibrosis. The combination of CCL4 with HFD induces extra level of fibrosis (ΔF). OCA, on the other, improves the fibrosis in the model to the extent that the remaining fibrosis is at the same level as induced by CCL4 alone (Figure 7.1). Given that OCA has no efficacy on the fibrosis induced by CCL4 alone, we suspect that ΔF is specific to the NASH model, hence suppressed by OCA.

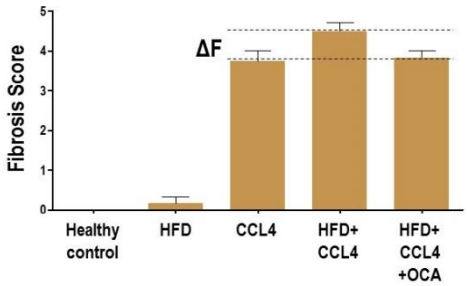

Figure 7.1. Fibrosis in healthy animals (fed on regular diet), those fed on HFD, treated with CCL4, and in the HFD+CCL4 NASH model with and without OCA treatment (from left to right, in order).

We sought to analyze the fibrosis in this NASH animal model, and collaborated with HistoIndex/Choutu to assess histopathology by coupled two-photon emission fluorescence (PTE) imaging with second harmonic generation (SHG) imaging. The automated SHG/TPE microscope identifies collagen (key component of fibrosis) in the SHG channel and the surrounding structures in the TPE channel directly from unstained tissue slides (formalin-fixed and paraffin-embedded). In the case of liver (biopsy) samples, a proprietary artificial intelligence (AI)-based algorithm recognizes and segregates the liver sections into different sub-anatomical areas. The fibrosis features are then identified and quantified from the SHG channel and, at the same time, other histopathological features in different areas are gathered from the TPE channel. The coupled SHG/TPE imaging, aided by AI-based analysis, affords a much less biased assessment of histopathology containing quantitative and sub-anatomical structural information.

In the initial attempt, the features of fibrosis from healthy, NASH model and NASH model treated with OCA were analyzed by SHG/TPE imaging (Figure 7.2). In the three sub-anatomical areas of the livers where fibrosis is observed in the NASH model; e.g., central vein, portal tract and peri-sinusoidal, the OCA treatment improves preferentially the fibrosis in the last two areas (Figure 7.2-A). When collagen fibers were analyzed by length and thickness, it was noted that the OCA treatment preferentially reduces long and thin strings (Figure 7.2-B and -C). When the steatosis features in the three sub-anatomical areas were analyzed, the outcome of OCA treatment on improvement of steatosis is more pronounced but without regional preference (Figure 7.3). Collectively, these preliminary results indicate that OCA exerts its anti-fibrotic effect with certain sub-regional preference, and that its anti-steatosis effect is more ubiquitous.

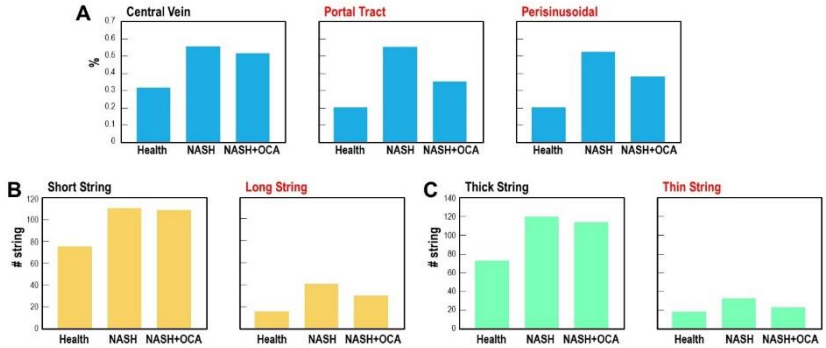

Figure 7.2. Quantitative histopathology analysis of fibrosis in the NASH model with and without OCA treatment by sub-anatomical areas (A), length (B) and thickness (C).

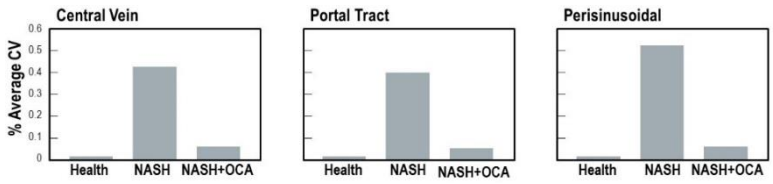

Figure 7.3. Quantitative histopathology analysis of steatosis in the NASH model with and without OCA treatment.

In the HFD+CCL4 model for NASH, a significant portion of the hepatic fibrosis is perilobular (mainly in zone 1); i.e., occurring around hepatic lobules, and bridged fibrosis between portal triads is pronounced. However, fibrotic septa are not common in this model. So the bridging fibers tend to be long and thin strings (Figure 7.4). When this model is used for efficacy test, compounds are usually administered at the same time CCL4 is injected intraperitoneally. Administered in this fashion, the OCA treatment prevents the bridging of perilobular fibers. The resulting fibers are usually short and loosened (Figure 7.4). These observations are largely consistent with the quantitative histopathology by the SHG/TPE imaging and AI analysis, supporting the notion that the HFD+CCL4 model bears histopathological features of clinical relevance to NASH.

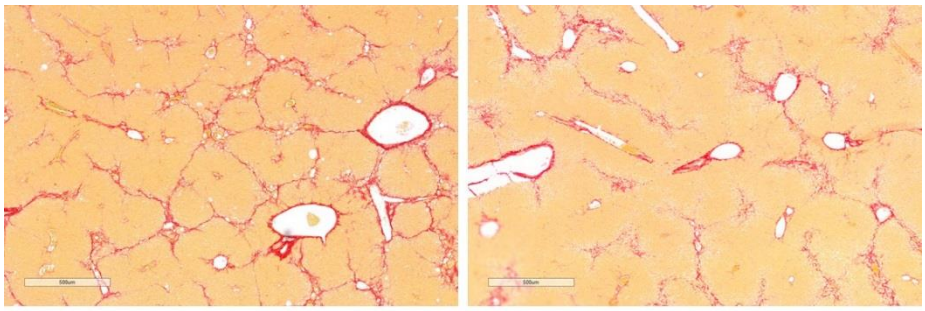

Figure 7.4. Histopathology of hepatic fibrosis in the HFD+CCL4 model with and without OCA treatment.

We have maintained a colony of cynomolgus monkeys that have been fed on high fat diet for ~4 years. Some of these monkeys have development symptoms that characteristic of NASH. In particular, perilobular bridging fibrosis/septa are observed, in addition to steatosis, inflammation and ballooning (Figure 7.5). Evidently, the bridging fibrosis in monkeys is distinct from that observed in the HFD+CCL4 model. Our pharmacological validation of the mouse model has demonstrated its clinical relevance and the use in efficacy study of NASH compounds in development, particularly for those with MOAs similar to OCA and MGL-3196. With the availability of monkey NASH model, compounds of different MOAs could be tested for in vivo efficacy.

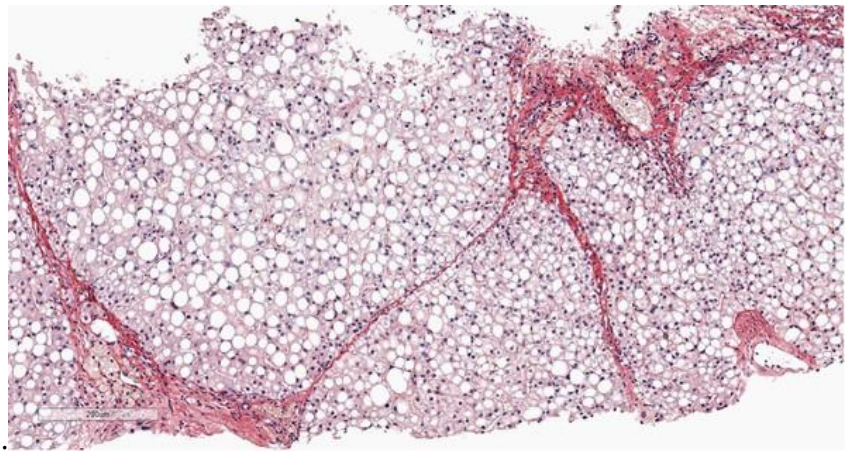

Figure 7.5. Histopathology of a monkey liver biopsy sample that is characteristic of NASH.

8. Case study: Application of AI to NASH Histopathology in Animal Model

In our analysis of liver histopathology, we use the NAS system for the clinical diagnosis of NASH, with scores of 0, 1, 2 and 3 assigned to steatosis and inflammation, and scores of 0, 1 and 2 assigned to ballooning. The assignment of score to histopathological findings is semi-quantitative and based on experience with complex features reduced to an integral number (i.e., zero dimension). Such a drastic reduction of content could make assessment of efficacy of compounds in development based on histopathology discriminatory without spectrum. We note that in the assessment of OCA efficacy on ballooning, the improvement is often variable (Figures 4.2-B and 6.1-A, and data not shown). We conducted a pilot study to apply artificial intelligence (AI) to restoring the complexity of histopathology of the NASH model. We trained machine learning (ML) for recognition of two such features, steatosis and ballooning, with rounds of manual interference, and asked ML to retrieve the size and the abundance (i.e., 2-D matrices) of both histopathological features in the livers of the HFD+CCL4 model.

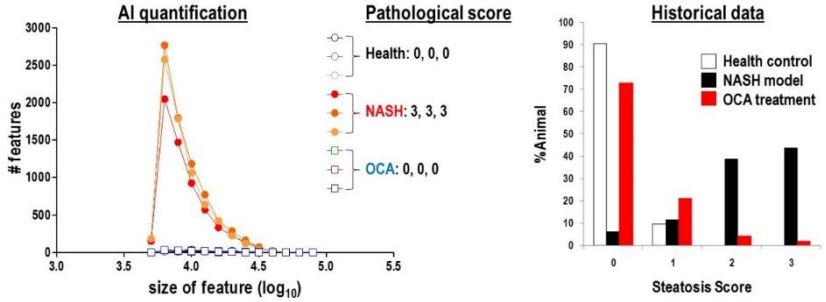

Figure 8.1. Histogram of distribution of steatosis by size (above a cut-off), as identified by AI, in livers from three animal groups, healthy control fed on regular diet (health), NASH model of HFD+CCL4 (NASH) and NASH model treated with OCA (OCA). Three animals were selected from each group, with their steatosis scores displayed in the middle. The right panel shows the distribution of steatosis by score, as determined by the histopathologist, of 50+ animals from each group from independent animal studies (i.e., historical data).

In the case of steatosis, the histograms of distribution (matrix) of three animal groups are distinctive and non-overlapping; i.e., lipid droplets are only seen in the NASH group. This consistent with the historical data of steatosis as determined by histopathology scoring that separates the peaks of NASH group from those of healthy control and NASH with OCA treatment (Figure 8.1), as the efficacy of OCA on improving steatosis could be determined with ease.

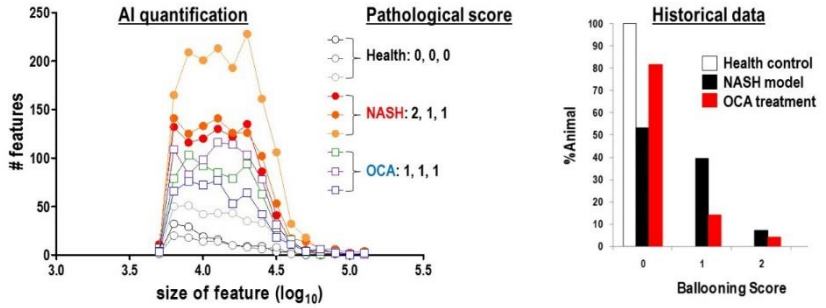

Figure 8.2. Histogram of distribution of ballooning by size (above a cut-off), as identified by AI (left), the corresponding histopathology scores of ballooning (middle) and historical data of distribution of balloon scores. The same set of animals as in Figure 8.1 were used for analyses.

In the case of ballooning (Figure 8.2), the AI analysis uncovered its complexity in the animal model. The ballooning matrices of the three animal groups are not as clearly separated. In the NASH group, the matrix of one of them (score of 2) is distinctive from the rest. However, the remaining two animals (score of 1) have much less ballooning features that their matrices are quantitatively close to those of model animals treated with OCA. Nonetheless in all three model animals treated with OCA (all of them with score of 1), the total ballooning features are quantitatively less than any of the three untreated animals. In this particular study, the scoring system barely distinguishes the model group from the treated group. However, the AI analysis clearly demonstrates the quantitative difference between these groups by individual animals. Although histopathology scoring gave 0 to all three animals in the healthy group, the AI analysis reveal residual ballooning in these animals. However their ballooning features are all less than two other groups. The difficulty associated with histopathology scoring in differentiating the model group and the treated group is further confirmed by the historical data, in which the peaks of three groups overlap with minor quantitative difference. These results indicate that the ballooning feature of this NASH model is heterogeneous, from individual animal to animal (even in the same group). Such heterogeneity may obscure the demonstration of OC efficacy by conventional histopathological scoring, arguing for more quantitative approach to such problem.

9. Case study: Pharmacodynamic Profiling of NASH Compounds

As observed in the efficacy study of combinational treatment, the pharmacological outcomes of two compounds are not necessarily predictable based on their MOAs (Figure 6.1). One of the possibilities for such unpredictability might be related to pharmacodynamic (PD) aspects of these compounds; i.e., the in vivo time course of effectors in response to the test compound upon administration. In this regard, the pharmacodynamic properties of a given compound are distinct from its MOA, in vitro potency or in vivo PK. They are the in vivo biological consequences to the compound treatment.

In the first experiment of a case study, we examined the time course of expression of the same gene (effector) in response to two compounds of slightly different MOAs (Figure 9.1-A). Even though the PK profiles of both compounds are similar (data not shown), the PD profiles are quite different. Compound 1 elicited a relatively quick response of increased expression of the effector gene, reaching to peak around 2 hour after administration. Its expression returned to basal level 6 hour after the peak. Compound 2, of a different MOA, elicited a different response of the same effector gene; i.e., after the initial induction, its expression was maintained an elevated Compound 1.

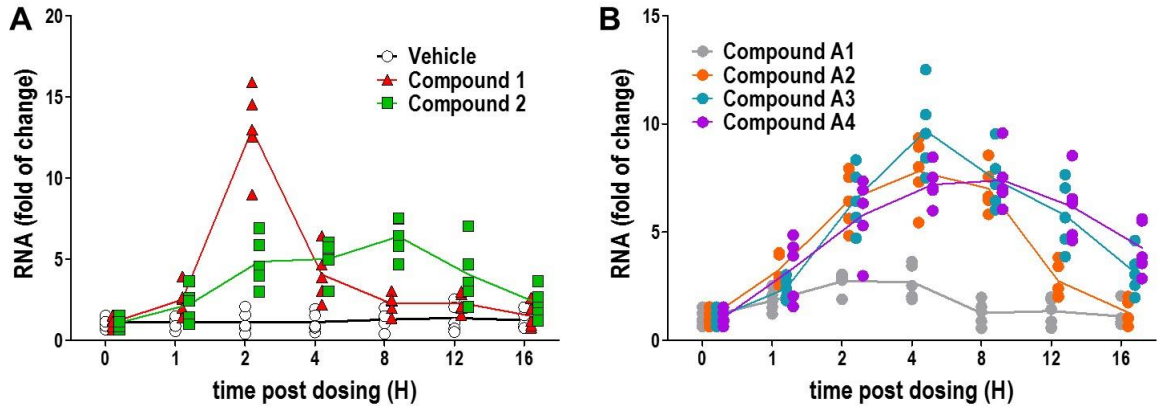

Figure 9.1. Pharmacodynamic profiling of compounds of different MOAs (A) and sample MO/target but of different chemical classes (B). The relative gene expression level is quantified by qRT-PCR and normalized by the relative level of RNA of vehicle group at time 0 (A) or that of untreated group at time 0 (B).

In the second experiment, four compounds of the same molecular target but different chemical classes were profiled. Although their potency and PK profiles are similar, the PD profile of Compound A1 was different from the rest. It elicited a low level of activation that lasted for 8 hours, whereas the activation elicited by Compounds A3 and A4 lasted at least 16 hours (the last time point), and that by Compound A1 12 hours (Figure 9.1-B).

These results demonstrate the need of PD profiling in understanding the in vivo properties of compounds for their biological consequences. Such profiling would be important when two compounds of different MOAs are combined for in vivo efficacy (synergistic or additive). How their PD profiles are paired and how the pharmacological outcomes are affected by such pairing will have to be determined experimentally in vivo, and in animal models that are suitable for both compounds.

10. Appendix: In Vivo Pharmacology Services at WuXi AppTec

The Department of Pharmacology in the Biology Business of WuXi AppTec is the largest of its kind in China, in terms of team size (~160 staff scientists, veterinarians, supporting technicians), R&D capabilities and experiences (Table 5), instrumentations, and animal facilities. Our Animal Care and Use Programs are fully accredited by AAALAC, and all animal studies are conducted according to the highest ethic and scientific standards. Our services cover all major therapeutic areas, metabolic and liver diseases, kidney diseases, digestive and gastrointestinal tract diseases, lung diseases, cardiovascular and hematological diseases, neurological diseases and pains, otological disease etc. – Table 5 offers an incomplete list of animal models and in life tests that are readily available at WuXi. Our disease pharmacology platforms employ animal models of rodents, NHP and other large animals. We have a histopathology, electrophysiology and in vitro laboratories affiliated with the platforms. In addition, we provide non-GLP toxicology support, safety pharmacology and in vivo tests in rodents and other animals. For any pharmacological inquiries, please contact us by email, pharmacology@wuxiapptec.com.

Table 5. List of animal models and in-life tests that are readily available at WuXi AppTec.

Metabolic and Liver Diseases	
T1 Diabetes	**Hyperlipidemia**
STZ-induced, mouse, rat & NHP	HCD induced hyperlipidemia & fibrosis, golden hamster
T2 Diabetes & Complications	HF/FD induced hyperlipidemia, NHP
HF/FD induced insulin resistance/diabetic NHP	P-407 induced hypertriglyeridemia, mouse
Diabetic ob/ob & db/db mice	Metabolic tests
ZDF rat model	Glucose tolerance tests, rodents, dog & NHP
Diabetic nephropathy, db/db mouse	Lipid tolerance test, rodents & NHP
Diabetic pain & ulcer foot, rat	Euglycemic clamp, rat & dog
Diabetic wound healing, rat	**Diet-Induced Obesity**
Acute Liver Injury	HFD induced obesity, mouse
APAP induced acute injury, mouse	HF/FD induced obesity, NHP
Liver Fibrosis	**Nonalcoholic Steatohepatitis (NASH)**
CCL4 induced fibrosis, rodents & NHP	HFD+CCL4 induced NASH, mouse
ANIT induced fibrosis, rat	HF/FD induced NAFLD/NASH, HNP
Bile duct ligation (BDL) induced fibrosis, rat	FPC induced NASH, mouse
TAA-induced fibrosis, rodents	MCD induced steatosis & fibrosis, mouse
HCD induced hyperlipidemia & fibrosis, golden hamster	nSTZ+HFD induced steatosis & fibrosis, mouse
Liver Infection	
HBV infection models	
Kidney Diseases	
Nephropathy	**Acute Kidney Injury**
Unilateral ureteral obstruction (UUO), mouse	Unilateral ischemia-reperfusion injury, NHP
Unilateral nephrectomy + HSD + aldosterone, rat	Cisplatin induced acute kidney injury, rodents
STZ + unilateral nephrectomy diabetic nephropathy, rat	Contrast agent induced acute kidney injury, rat
Unilateral nephrectomy in db/db mouse	
5/6 Nephrectomy	
Digestive and Gastrointestinal Tract Diseases	
Gastric ulcer	**Inflammatory Bowel Diseases**
Acetic acid induced gastric mucosal lesion, rat	DSS induced ulcerative colitis, rodents & NHP
GI Tract Infection	TNBS/Oxazolone induced Crohn's disease, rodents & HNP
Gastrointestinal tract infection of *C. difficile*, mouse	Colitis, T-cell transfer in RAG-/- or SCID mouse
Lung Diseases	
Pulmonary Fibrosis	**Pulmonary Artery Hypertension (PAH)**
Bleomycin induced idiopathic fibrosis, mouse	Monocrotaline (MCT) induced PAH, rat

SiO_2 induced fibrosis, mouse	**Acute Lung Injuries (ALI)**
Asthma & COPD	Cigarette smoke induced ALI, mouse
OVA/HDM induced asthma, rodents & guinea pig	Cigarette smoke + LPS induced ALI, rat
Cigarette smoke induced COPD, rodents	DK-PGD2 induced eosinophile-mediated ALI, rat
Pulmonary Infections	**Other Models**
IFV and RSV pulmonary infections, mouse	Ovalbumin induced allergic rhinitis, rat
Bacterial pulmonary infections, mouse	Citric acid induced cough, guinea pig
	Obstructive sleep apnea hypopnea syndrome (OSAHS), DIO mouse
Cardiovascular and Hematological Diseases	
Heart Failure	**Atherosclerosis**
Myocardial infarction (MI) and reperfusion injury IR), rodents, NHP	Diet induced atherosclerosis in ApoE-/- mous
TAC induced cardiac hypertrophy and heart failure, mouse	**Thrombosis and Hematological Diseases**
Angiotensin II-induced heart failure with preserved ejection fraction	Arteriovenous shunt, rat
Pulmonary Artery Hypertension (PAH)	$FeCl_3$ induced carotid artery thrombosis, rat
Monocrotaline (MCT) induced PAH, rat	Tail bleeding, rat
Ischemic Stroke and Brain Injury	Platelet aggregation assay, rodents & NHP
Middle cerebral artery occlusion (MCAO) model for cerebral infarction and ischemic reperfusion injury (CIRI)	Hemagglutination test, rodents & NHP
	Disseminated intravascular coagulation, rabbit
Four-vessel occlusion (4-VO) induced global ischemia, rat	Hyperfibrinolysis, rat
Traumatic brain injury, rat	
Neurological Diseases and Pains	
Neurodegenerative Diseases	**Pains**
APP/PS1 transgenic model for Alzheimer's Disease	Acute inflammatory pain: formalin, carrageenan, post-surgery, capsaicin
Unilateral 6-OHDA lesion model for Parkinson's Disease	
MPTP induced Parkinson's Disease model	Chronic inflammatory pain: complete Freund's adjuvant, carrageenan
L-DOPA induced dyskinesia in Parkinson's Disease model	Acute nociception: tail flick, hot plate
Other Degenerative Disease/Pain	Chronic neuropathic pain: spinal nerve light (Chung), chronic constriction injury, partial sciatic nerve ligation, spared nerve injury, chemotherapy induced peripheral neurotoxicity, bone cancer pain
MIA induced osteoarthritis, rat	
MOG induced experimental autoimmune encephalomyelitis, mouse	Fibromyalgia-like pain: intermittent cold stress model
Attention Deficit Hyperactivity	Itch
Neonatal 6-OHDA induced ADHA, rat	Sunburn
Anxiety and Depression	**Motor Functions**
Forced swimming test	Spontaneous locomotors activity test
Vogal conflict test	Drug evoked locomotors activity test
Learnt helplessness test	Rotarod test
Schizophrenia	Weight bearing test
Prepulse inhibition test	Grip force test
Conditional avoidance response test	**Others**
Hyperalgesia	Attention set-shifting test
Thermal hyperalgesia test	Tactile allodynia test
Mechanical hyperalgesia test	Paw thickness/volume test
Cold hyperalgesia test	